

Frequency-Dependent Sliding-Mode Control of Galfenol-Driven Unimorph Actuator Based on Finite-Element Model

Liang Shu, Marcelo Dapino, Guichu Wu, and Dingfang Chen

Abstract—A dynamic model is presented by coupling the structural dynamics of a Galfenol-driven unimorph beam with the magnetostriction generated by the active layer. Weak form equations are obtained by employing the virtual work principle, and finite-element representation of the model is implemented through a Galerkin discretization. In order to facilitate the design of the controller, a linearized constitutive law is used to describe the magnetostriction of Galfenol. A finite-dimensional sliding-mode controller is developed which accounts for the frequency-dependent deviations of structural damping and the piezomagnetic constant. A nonlinear switch controller, combined with the equivalent controller, is developed to guarantee Lyapunov stability at different frequencies, without changing the initial parameters of the controller. Since the model is finite-dimensional, model parameters are nonlinearly coupled in the state and output matrices in the state-space equation. A genetic algorithm is employed to solve the nonlinear estimation problem. Experimental results show that the model parameters are almost constant below 220 Hz. The model parameters are frequency dependent above 220 Hz. It is also found that significant performance enhancements are achieved by the proposed control relative to conventional Proportional-Integral (PI) control. The system remains stable for frequencies up to 400 Hz.

Index Terms—Actuator dynamics, finite-element model, Galfenol, sliding-mode control.

Manuscript received November 23, 2014; revised March 20, 2015, April 25, 2015, and July 9, 2015; accepted August 20, 2015. Date of publication September 22, 2015; date of current version January 8, 2016. This work was supported in part by the National Natural Science Foundation of China under Grant 51205293 and Grant 51175395, in part by the Natural Science Foundation of Zhejiang Province under Grant LY15E050011, and in part by the China Postdoctoral Science Foundation under Grant 2015M571904.

L. Shu and G. Wu are with the Key Laboratory of Low-Voltage Apparatus Intellectual Technology of Zhejiang, Wenzhou University, Wenzhou 325027, China (e-mail: liang.shu9@gmail.com; wgc@wzu.edu.cn).

M. Dapino is with the Department of Mechanical and Aerospace Engineering, The Ohio State University, Columbus, OH 43210 USA (e-mail: dapino.1@osu.edu).

D. Chen is with the Institute of Intelligent Manufacturing and Control, Wuhan University of Technology, Wuhan 430063, China (e-mail: dfchen@whut.edu.cn).

Color versions of one or more of the figures in this paper are available online at <http://ieeexplore.ieee.org>.

Digital Object Identifier 10.1109/TIE.2015.2480376

I. INTRODUCTION

MAGNETOSTRICTIVE materials are considered for applications in which small but precise deformations are required [1], [2], [4], [24]. These materials deform when exposed to magnetic fields and undergo magnetization changes in response to stress [7], [9]. Galfenol is a magnetostrictive material which exhibits moderate magnetically induced strain (about 400 ppm) and intrinsic steel-like structural properties. Since Galfenol can be safely loaded with normal or shear stresses (up to 500 MPa in tension), it can operate as a sensor or actuator located in the load path. However, Galfenol is nonlinear due to saturation and hysteresis in its response to applied field and stress. Moreover, under a.c. excitation, Galfenol's high electrical conductivity comparable to that of steel makes it susceptible to eddy current losses. High-performance Galfenol systems can be challenging to design and control.

An effective approach to solve the nonlinear problem is open loop compensation, in which a nonlinear inverse filter is constructed to linearize the hysteresis system [14], [15], [21], [25], [32]. The inverse filter is implemented by numerically inverting the nonlinear constitutive material model. Examples of this approach include the homogenized energy model [14], [15], Preisach model [21], [25], [26], [32], Jiles-Atherton model [22] or Prandtl-Ishlinskii model [3], [10]. Nonlinear inverse compensators which approximately linearize the constitutive behavior rely on accurate models and relatively simple control methods. However, Galfenol models that accurately describe the effects of hysteresis, field and stress dependencies, and frequency dependence tend to be complex. Further, the computational complexity of inverting a nonlinear constitutive law generally complicates the application of inverse compensators under a.c. excitations [17].

Nonlinear control strategies without inverse compensation have also been attempted. Extreme precise motion tracking of a piezoelectric positioning stage was studied in [28] using sampled-data iterative learning control (ILC). The dynamics of the system were approximated with the product of 6 groups of second-order transfer functions. In [8] modeling and a robust control strategy were studied for piezoelectric microgripper. A mixed high authority control (HAC) and low authority control (LAC) strategy was used to regulate hysteresis subjected to uncertainties. System dynamics were modeled as the summation of a linear electromechanical equation and a nonlinear operator that included hysteresis and the creep. However, the model only had 2 degrees of freedom (DOFs), which was inadequate to

fully describe the dynamics of a flexible structure. In [19] the tip tracking control of a Timoshenko micro-cantilever beam was investigated. Dynamic equations of the beam were developed using the Hamilton principle. The cascade control method was studied based on Galerkin discretization of the model and simulation results were discussed. However, the performance of the controller was not substantiated experimentally. A nonlinear optimal control method was proposed by Oates and Smith [17] in which the control signal was determined directly by optimizing a nonlinear cost function. A Kalman filter was developed to estimate unobservable states in the perturbed optimality system. Since the accuracy of a Kalman filter mostly depends on the model parameters, control performance could be affected if the parameters are frequency dependent. A similar nonlinear control was developed in which the open loop nonlinear component was computed off-line [16]. Experimental tests were conducted by coupling the nonlinear component with PI perturbation feedback. Since the PI feedback reduced the operating uncertainties, control performance was improved compared with open loop nonlinear compensation. Chen *et al.* [5] developed a 1-D adaptive controller for systems with hysteresis. The parameters needed for operation of the controller were adaptively estimated online. However, the controller was limited to 1-D systems. Practical perturbations were not considered and experimental tests have not been conducted to verify the adaptive framework.

Sliding-mode control has been extensively adopted to control nonlinear systems [6], [29], [30]. A robust sliding-mode controller was developed by Panusittikorn and Ro [18] to control a magnetostrictive tool servo system. The controller was limited to 1-D applications, and high frequencies were not considered in the experiments. Sliding-mode controllers have also been implemented for piezoelectric transducers [11], [13], [27]. In order to estimate immeasurable states, state observers were developed to approximate unknown states and disturbances [11], [27]. Structural dynamics were modeled as simple second order systems, and only specified frequency ranges were verified experimentally. An enhanced sliding-mode controller was developed by Liaw [13] to accommodate parametric uncertainties and nonlinearities, including hysteresis and un-modeled dynamics. The design process was based on a 1-D second order system, and the bounds of the uncertainties were assumed to be known in advance. In physical magnetostrictive systems, however, model parameters change with frequency. In addition, since eddy current effects depend not only on frequency but also on magnetic flux dynamics, system dynamics change even if the system is excited at a constant frequency. Moreover, 1-D second order equations are inadequate to describe continuous flexible structure dynamics. In order to describe the system dynamics of Galfenol unimorph actuators, 1-D second order equations need to be extended to be finite-dimensional.

This paper aims to find a finite-dimensional control solution of Galfenol unimorph actuators for dynamic applications without solving the complex nonlinear constitutive model. Usually Galfenol models that accurately describe the effects of hysteresis, field and stress dependencies, and frequency dependence tend to be complex. Solving this complex constitutive model in real time control is usually impractical due to the limit of the sampling frequency and the calculation speed of micro-

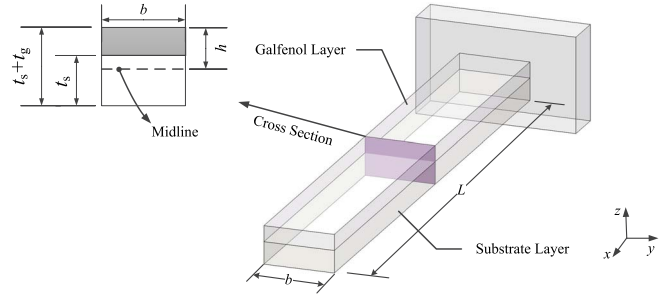


Fig. 1. Magnetostrictive composite beam.

controller unit (MCU), especially for dynamic applications. In order to reduce computational burden, we use a linearized constitutive law to describe the magnetostriction of Galfenol. A finite-dimensional sliding-mode controller is developed to compensate the modeling error due to the influence of hysteresis and frequency-dependent parameter uncertainties. The sliding surface is defined based on finite-dimensional dynamic equations rather than second order transfer functions. Parameter deviations due to frequency dependence are estimated with nonlinear Genetic Algorithms. Experimental tests are conducted at frequencies, ranging from 30 Hz to 400 Hz, without changing the initial model parameters.

II. FINITE-DIMENSIONAL MODEL

A composite beam consisting of a Galfenol layer bonded to a nonmagnetic substrate is clamped at one end while the other end is free (Fig. 1). The $x - y$ plane of the coordinate system is set on the midplane of the beam. The composite beam is assumed to have length L and width b having a Galfenol layer of thickness t_g , modulus E_g , and mass density ρ_g perfectly bonded to the substrate with thickness t_s , modulus E_s , and mass density ρ_s . When a magnetic field H is applied along the x direction, bending is induced due to the magnetostriction $\lambda(\sigma_g, H)$ generated in the Galfenol layer. The stress in the substrate σ_s is assumed to follow Hooke's law, $\sigma_s = E_s \varepsilon_s$. The total strain in the Galfenol layer ε_g is the sum of the elastic strain and the magnetostriction. The internal stress in the Galfenol layer can thus be expressed as

$$\sigma_g = E_g (\varepsilon_g - \lambda(\sigma_g, H)). \quad (1)$$

For the magnetostrictive bender actuator illustrated in Fig. 1, the strain is the superposition of the extensional strain and bending strain

$$\varepsilon = \frac{\partial u(t, x)}{\partial x} - z \frac{\partial^2 v(t, x)}{\partial x^2} \quad (2)$$

where $u(t, x)$ denotes the horizontal displacement of the midplane and $v(t, x)$ denotes its vertical displacement. In order to develop a finite-dimensional governing equation, the virtual work principle is employed. The sum of the virtual work done by internal and external forces is zero

$$-\delta W_i - \delta W_e = 0 \quad (3)$$

where δW_i denotes internal virtual work and δW_e denotes external virtual work. The virtual work principle has been used

to model the nonlinear magnetoelastic coupling of Galfenol unimorphs [20]. The hysteretic behavior of Galfenol was described with a discrete energy-averaged model and the weak form equations were discretized through finite-element discretization. In this paper, a similar modeling framework is used to develop a finite-dimensional model. To reduce computational burden, the discrete energy-averaged model is replaced with a linearized constitutive law for the magnetostriction

$$\lambda = \tilde{d}H \quad (4)$$

$$H = \tilde{N}I_c \quad (5)$$

where \tilde{d} is the linear piezomagnetic strain coefficient, \tilde{N} is the number of turns per length of coil, and I_c is the excitation current. Weak form equations derived from the virtual work principle are discretized through the Galerkin method. The beam is discretized into N_e elements. Each node has 3 DOFs. The values of the DOFs associated with the vertical displacement for a single element are denoted \mathbf{q}_e^v , in which the first two components are the vertical displacement and rotation of the left node and the second two are the vertical displacement and rotation of the right node. The values of the DOFs associated with the horizontal displacement for a single element are denoted \mathbf{q}_e^u where the first entry is the horizontal displacement of the left node and the second entry is the horizontal displacement of the right node. The assembled finite-dimensional equation is

$$\begin{bmatrix} \mathbf{m}_e^u & 0 \\ 0 & \mathbf{m}_e^v \end{bmatrix} \begin{bmatrix} \ddot{\mathbf{q}}_e^u \\ \ddot{\mathbf{q}}_e^v \end{bmatrix} + \tilde{c} \begin{bmatrix} \mathbf{c}_e^u & 0 \\ 0 & \mathbf{c}_e^v \end{bmatrix} \begin{bmatrix} \dot{\mathbf{q}}_e^u \\ \dot{\mathbf{q}}_e^v \end{bmatrix} + \begin{bmatrix} \mathbf{k}_e^u & -(\mathbf{k}_e^{uv})^T \\ -(\mathbf{k}_e^{uv}) & \mathbf{k}_e^v \end{bmatrix} \begin{bmatrix} \mathbf{q}_e^u \\ \mathbf{q}_e^v \end{bmatrix} = \tilde{d} \begin{bmatrix} \mathbf{f}^u \\ \mathbf{f}^v \end{bmatrix} \quad (6)$$

where \tilde{c} denotes system damping. Since a linear constitutive law is employed in the material model, \tilde{c} and \tilde{d} need to be estimated over a range of frequencies considering system nonlinearities and frequency dependencies. Further details on system model (6) are given in Appendix A. N_e denotes the element numbers and it will matter when the element matrices in Appendix A are globally assembled.

III. SLIDING-MODE CONTROL BASED FINITE-DIMENSIONAL MODEL

A. State-Space Formulation

For convenience, (6) is implemented in state-space form. We define $\mathbf{w} = [\mathbf{q}_e^u, \mathbf{q}_e^v]^T$ and the state variable as

$$\mathbf{X}(t) = \begin{bmatrix} \{\mathbf{w}\} \\ \{\dot{\mathbf{w}}\} \end{bmatrix} = \begin{bmatrix} \mathbf{x}_1(t) \\ \mathbf{x}_2(t) \end{bmatrix}$$

where $\mathbf{x}_1(t) \in \mathbf{R}^{3n \times 1}$, $\mathbf{x}_2(t) \in \mathbf{R}^{3n \times 1}$. The state-space equation of the dynamic model can be expressed as

$$\begin{aligned} \dot{\mathbf{X}}(t) &= \mathbf{A}\mathbf{X}(t) + \mathbf{B}I_c(t) \\ y(t) &= \mathbf{\Gamma}\mathbf{X}(t) \end{aligned} \quad (7)$$

with

$$\mathbf{A} = \begin{bmatrix} \mathbf{0}_{3n \times 3n} & \mathbf{I} \\ -[\mathbf{M}]^{-1}[\mathbf{K}] & -\tilde{c}[\mathbf{M}]^{-1}[\mathbf{C}] \end{bmatrix}, \mathbf{B} = \begin{bmatrix} \mathbf{0}_{3n \times 1} \\ -\tilde{d}[\mathbf{M}]^{-1}[\mathbf{F}] \end{bmatrix}.$$

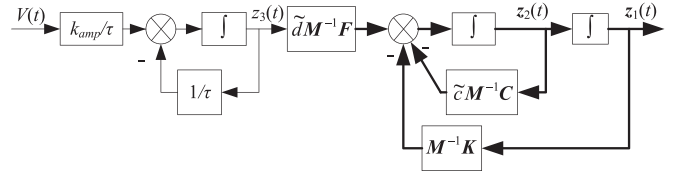


Fig. 2. Block structure of the state-space model.

\mathbf{M} , \mathbf{C} , \mathbf{K} are the mass, damping, and stiffness matrices, and \mathbf{F} is the load vector. The output matrix $\mathbf{\Gamma}$ is determined by the state which needs to be controlled. If the state variable to be tracked is located at the j th entry of $\mathbf{X}(t)$ and i th node of the discretized beam ($j = 1, 2, 3, 4, 5, 6$), $\mathbf{\Gamma}$ can be expressed as

$$\mathbf{\Gamma} = [\mathbf{0}_{1 \times 6(i-1)} \langle j-1 \rangle^{-1} \langle j-2 \rangle^{-1}, \dots, \langle j-6 \rangle^{-1} \mathbf{0}_{1 \times 6(n-i)}]$$

where $\langle \cdot \rangle^{-1}$ is the singular function which is defined as

$$f(x) = \langle x - a \rangle^{-1} = \begin{cases} 0, & x \neq a \\ 1, & x = a. \end{cases}$$

A voltage-current model is needed to account for the applied control signal being a voltage rather than current. The equivalent circuit can be modeled as an inductor-resistor (LR) series circuit, which can be expressed as

$$\frac{dI_c(t)}{dt} = -\frac{1}{\tau}I_c(t) + \frac{k_{\text{amp}}}{\tau}V(t) \quad (8)$$

where $V(t)$ is the control voltage, τ is the time constant and k_{amp} is the steady-state gain. In order to write the state-space equation in terms of control voltage, a new state variable is defined as

$$\mathbf{Z}(t) = \begin{bmatrix} \mathbf{z}_1(t) \\ \mathbf{z}_2(t) \\ \mathbf{z}_3(t) \end{bmatrix} = \begin{bmatrix} \mathbf{x}_1(t) \\ \mathbf{x}_2(t) \\ I_c(t) \end{bmatrix}.$$

Coupling (8) with (7) one obtains

$$\begin{aligned} \dot{\mathbf{Z}}(t) &= \mathbf{H}\mathbf{Z}(t) + \mathbf{T}V(t) \\ y(t) &= \mathbf{P}\mathbf{Z}(t) \end{aligned} \quad (9)$$

where $\mathbf{H} \in \mathbf{R}^{(6n+1) \times (6n+1)}$, $\mathbf{T} \in \mathbf{R}^{(6n+1) \times 1}$, $\mathbf{P} \in \mathbf{R}^{1 \times (6n+1)}$

$$\mathbf{H} = \begin{bmatrix} \mathbf{0} & \mathbf{I} & \mathbf{0}_{3n \times 1} \\ -[\mathbf{M}]^{-1}[\mathbf{K}] & -\tilde{c}[\mathbf{M}]^{-1}[\mathbf{C}] & \tilde{d}[\mathbf{M}]^{-1}\mathbf{F} \\ \mathbf{0}_{1 \times (3n)} & \mathbf{0}_{1 \times (3n)} & -\frac{1}{\tau}\mathbf{1} \times \mathbf{1} \end{bmatrix}$$

$$\mathbf{T} = \begin{bmatrix} \mathbf{0}_{3n \times 1} & \mathbf{0}_{3n \times 1} & \frac{k_{\text{amp}}}{\tau} \end{bmatrix}^T, \mathbf{P} = [\mathbf{\Gamma}_{1 \times 6n} \quad \mathbf{0}_{1 \times 1}].$$

B. Equivalent Control

The tip displacement is the selected state variable to be tracked. The equivalent controller is developed first in the sliding-mode design [31]. The block diagram of (9) is illustrated in Fig. 2. It is seen from Fig. 2 that $\mathbf{z}_1(t)$ and $\mathbf{z}_2(t)$ are directly coupled via matrices $\tilde{c}\mathbf{M}^{-1}\mathbf{C}$ and $\mathbf{M}^{-1}\mathbf{K}$, while $\mathbf{z}_1(t)$ and $\mathbf{z}_3(t)$ are indirectly coupled. This indirect coupling will

generate a zero matrix if the control signal is solved directly from (9). In fact, if the sliding surface is defined as

$$\begin{aligned} s(t) &= g_1 e(t) + g_2 \dot{e}(t) = [g_1 \quad g_2] \begin{bmatrix} r(t) - y(t) \\ \dot{r}(t) - \dot{y}(t) \end{bmatrix} \\ &= [g_1 \quad g_2] \begin{bmatrix} r(t) - \mathbf{PZ}(t) \\ \dot{r}(t) - \mathbf{PHZ}(t) - \mathbf{PTV}(t) \end{bmatrix} \end{aligned} \quad (10)$$

where $e(t)$ denotes the tracking error, $r(t)$ denotes the reference signal, g_1 and g_2 are the design parameters, then the matrix product \mathbf{PT} in (10) turns out to be zero since $\mathbf{z}_1(t)$ and $\mathbf{z}_3(t)$ are indirectly coupled. In order to solve this problem, a new output matrix is defined as

$$\begin{aligned} y(t) &= \mathbf{C}_1 \mathbf{Z}(t) \\ \dot{y}(t) &= \mathbf{C}_2 \dot{\mathbf{Z}}(t) = \mathbf{C}_3 \mathbf{x}_2(t). \end{aligned} \quad (11)$$

The second derivative of $y(t)$ can be solved as

$$\begin{aligned} \ddot{y}(t) &= \mathbf{C}_3 \dot{\mathbf{x}}_2(t) \\ &= \mathbf{C}_3 [-\mathbf{M}^{-1} \mathbf{Kz}_1(t) - \tilde{c} \mathbf{M}^{-1} \mathbf{Cz}_2(t) + \tilde{d} \mathbf{M}^{-1} \mathbf{Fz}_3(t)] \\ &= \mathbf{C}_4 \dot{\mathbf{Z}}(t) \end{aligned} \quad (12)$$

where

$$\begin{aligned} \mathbf{C}_1 &= [\mathbf{0}_{1 \times 6(n-1)} \quad 0 \quad 1 \quad \mathbf{0}_{1 \times 5}] \\ \mathbf{C}_2 &= [\mathbf{0}_{1 \times 6(n-1)} \quad 0 \quad 0 \quad 0 \quad 0 \quad 1 \quad 0 \quad 0] \\ \mathbf{C}_3 &= [\mathbf{0}_{1 \times 3(n-1)} \quad 0 \quad 1 \quad 0] \\ \mathbf{C}_4 &= [-\mathbf{C}_3 \mathbf{M}^{-1} \mathbf{K} \quad -\tilde{c} \mathbf{C}_3 \mathbf{M}^{-1} \mathbf{C} \quad \tilde{d} \mathbf{C}_3 \mathbf{M}^{-1} \mathbf{F}]. \end{aligned}$$

We now define the sliding surface as

$$\begin{aligned} s(t) &= g_1 e(t) + g_2 \dot{e}(t) + g_3 \ddot{e}(t) \\ &= [g_1 \quad g_2 \quad g_3] \begin{bmatrix} r(t) - \mathbf{C}_1 \mathbf{Z}(t) \\ \dot{r}(t) - \mathbf{C}_2 \dot{\mathbf{Z}}(t) \\ \ddot{r}(t) - \mathbf{C}_4 \dot{\mathbf{Z}}(t) \end{bmatrix} \\ &= \mathbf{G} [\mathbf{R} - \tilde{\mathbf{A}} \mathbf{Z}(t)]. \end{aligned} \quad (13)$$

The derivative with respect to time in (13) is

$$\dot{s}(t) = \mathbf{G} [\dot{\mathbf{R}}(t) - \tilde{\mathbf{A}} \dot{\mathbf{Z}}(t)] \quad (14)$$

where

$$\begin{aligned} \mathbf{R} &= [r(t) \quad \dot{r}(t) \quad \ddot{r}(t)]^T, \mathbf{G} = [g_1 \quad g_2 \quad g_3] \\ \tilde{\mathbf{A}} &= [\mathbf{C}_1 \quad \mathbf{C}_2 \quad \mathbf{C}_4]^T. \end{aligned}$$

Substitution of (9) into (14) gives

$$\begin{aligned} \dot{s}(t) &= \mathbf{G} (\dot{\mathbf{R}}(t) - \tilde{\mathbf{A}} \dot{\mathbf{Z}}(t)) \\ &= \mathbf{G} \dot{\mathbf{R}}(t) - \mathbf{G} \tilde{\mathbf{A}} \mathbf{HZ}(t) - \mathbf{G} \tilde{\mathbf{A}} \mathbf{T} V(t). \end{aligned} \quad (15)$$

The equivalent control signal can be obtained by setting (15) equal to zero

$$V_{\text{eq}}(t) = (\mathbf{G} \tilde{\mathbf{A}} \mathbf{T})^{-1} [\mathbf{G} \dot{\mathbf{R}}(t) - \mathbf{G} \tilde{\mathbf{A}} \mathbf{HZ}(t)]. \quad (16)$$

It can be seen from (16) that the equivalent control signal depends on the mapping matrix $\tilde{\mathbf{A}}$ and state matrix \mathbf{H} , which are frequency dependent. Instability will be induced if the same matrix values are used in the control signal $V_{\text{eq}}(t)$ at different

frequencies. In order to improve the robustness of the sliding-mode controller, the parameter deviations due to frequency dependency should be considered. Moreover, full state feedback is not available in (16) since the rotation of a beam element and horizontal displacement cannot be measured. The states that can be measured are vertical displacement and the excitation current, which means the states that are immeasurable need to be generated from the model. Modeling errors need to be considered in the robust controller design.

C. Stability Analysis and Robust Design

It is assumed that the mapping matrix $\tilde{\mathbf{A}}$ and state matrix \mathbf{H} change with frequency. Only the initial values $\tilde{\mathbf{A}}_0$ and \mathbf{H}_0 are known. Equation (16) can be expressed in terms of initial values as

$$V_{\text{eq}}(t) = (\mathbf{G} \tilde{\mathbf{A}}_0 \mathbf{T})^{-1} [\mathbf{G} \dot{\mathbf{R}}(t) - \mathbf{G} \tilde{\mathbf{A}}_0 \mathbf{H}_0 \mathbf{Z}_0(t)] \quad (17)$$

where $\mathbf{Z}_0(t)$ denotes the states generated from the model. In order to obtain the Lyapunov asymptotic stability, a nonlinear component $u_f(t)$ is needed to suppress the uncertainties due to the frequency dependence of \tilde{c} and \tilde{d} . The control law is proposed as

$$\begin{aligned} V(t) &= V_{\text{eq}}(t) + u_f(t) \\ &= V_{\text{eq}}(t) + \epsilon \operatorname{sgn}(s(t)) \end{aligned} \quad (18)$$

where ϵ is the control variable. Robust design can be implemented via Lyapunov's second method. The Lyapunov candidate function is defined as

$$V_l(t) = \frac{1}{2} s(t) s(t)^T. \quad (19)$$

The derivative of the Lyapunov function is

$$\dot{V}_l(t) = s(t) \dot{s}(t). \quad (20)$$

The derivative of the sliding surface can be obtained by combining (15)–(18)

$$\begin{aligned} \dot{s}(t) &= \mathbf{G} \dot{\mathbf{R}}(t) - \mathbf{G} \tilde{\mathbf{A}} \mathbf{HZ}(t) \\ &\quad - \mathbf{G} \tilde{\mathbf{A}} \mathbf{T} \left((\mathbf{G} \tilde{\mathbf{A}}_0 \mathbf{T})^{-1} (\mathbf{G} \dot{\mathbf{R}}(t) - \mathbf{G} \tilde{\mathbf{A}}_0 \mathbf{H}_0 \mathbf{Z}_0(t)) \right. \\ &\quad \left. + \epsilon \operatorname{sgn}(s(t)) \right) \\ &= (\mathbf{G} - \mathbf{G} \tilde{\mathbf{A}} \mathbf{T} (\mathbf{G} \tilde{\mathbf{A}}_0 \mathbf{T})^{-1} \mathbf{G}) \dot{\mathbf{R}}(t) - \mathbf{G} \tilde{\mathbf{A}} \mathbf{HZ}(t) \\ &\quad + \mathbf{G} \tilde{\mathbf{A}} \mathbf{T} (\mathbf{G} \tilde{\mathbf{A}}_0 \mathbf{T})^{-1} \mathbf{G} \tilde{\mathbf{A}}_0 \mathbf{H}_0 \mathbf{Z}_0(t) - \mathbf{G} \tilde{\mathbf{A}} \mathbf{T} \epsilon \operatorname{sgn}(s(t)) \\ &= \mathbf{G}^* \dot{\mathbf{R}}(t) + \Psi - \mathbf{G} \tilde{\mathbf{A}} \mathbf{T} \epsilon \operatorname{sgn}(s(t)) \end{aligned} \quad (21)$$

where $\Psi = \mathbf{G} \tilde{\mathbf{A}} \mathbf{T} (\mathbf{G} \tilde{\mathbf{A}}_0 \mathbf{T})^{-1} \mathbf{G} \tilde{\mathbf{A}}_0 \mathbf{H}_0 \mathbf{Z}_0(t) - \mathbf{G} \tilde{\mathbf{A}} \mathbf{HZ}(t)$, $\mathbf{G}^* = \mathbf{G} - \mathbf{G} \tilde{\mathbf{A}} \mathbf{T} (\mathbf{G} \tilde{\mathbf{A}}_0 \mathbf{T})^{-1} \mathbf{G}$. Substitution of (21) into (20) gives

$$\begin{aligned} \dot{V}_l(t) &= s(t) \dot{s}(t) \\ &= s(t) \mathbf{G}^* \dot{\mathbf{R}}(t) + s(t) \Psi - \mathbf{G} \tilde{\mathbf{A}} \mathbf{T} \epsilon |s(t)| < 0. \end{aligned} \quad (22)$$

The sign of $\mathbf{G} \tilde{\mathbf{A}} \mathbf{T}$ is positive due to the physical meaning of the modeling parameters. Thus the switching term in (22) should

satisfy

$$\epsilon > (\mathbf{G}\tilde{\mathbf{A}}\mathbf{T})^{-1} \left| \mathbf{G}^* \dot{\mathbf{R}}(t) + \Psi \right|. \quad (23)$$

Lyapunov asymptotic stability can be obtained as long as (23) is satisfied. In order to ensure the stability of the sliding surface proposed in (13), the parameter vector \mathbf{G} is selected as Hurwitz polynomial coefficients, which means the coefficients are positive real numbers and the roots are located in the left half-plane of the complex plane. It can be seen from (23) that ϵ depends on the parameters $\tilde{\mathbf{A}}$, \mathbf{H} and states $\mathbf{Z}(t)$. Since the control signal $V(t)$ is the sum of u_f and V_{eq} , the performance of the proposed controller can be directly affected by the choice of ϵ . Other work [12], [23] has taken ϵ as a constant that is large enough to satisfy (23). However, considerable chatter, even instability, may be induced if ϵ is too large. In order to determine ϵ , the relationship between \tilde{c} , \tilde{d} and ϵ must be analyzed. The following assumptions are made:

$$\begin{aligned} \mathbf{Z}(t) &= \mathbf{Z}_0(t) - \Delta\mathbf{Z}(t), \quad \tilde{\mathbf{A}} = \tilde{\mathbf{A}}_0 - \Delta\tilde{\mathbf{A}}, \quad \mathbf{H} = \mathbf{H}_0 - \Delta\mathbf{H} \\ \tilde{c} &= \tilde{c}_0 - \Delta\tilde{c}, \quad \tilde{d} = \tilde{d}_0 - \Delta\tilde{d}, \quad \tilde{c}_0 \in [\tilde{c}_l \ \tilde{c}_u] \\ \tilde{d}_0 &\in [\tilde{d}_l \ \tilde{d}_u] \end{aligned} \quad (24)$$

where the subscript l denotes the lower bound of the deviation and u denotes the upper bound. Thus, \mathbf{G}^* can be rewritten in terms of parameter deviations by employing (24)

$$\begin{aligned} \mathbf{G}^* &= \mathbf{G} - \mathbf{G}\tilde{\mathbf{A}}\mathbf{T}(\mathbf{G}\tilde{\mathbf{A}}_0\mathbf{T})^{-1}\mathbf{G} = \mathbf{G} - \mathbf{G}(\mathbf{G}\tilde{\mathbf{A}}\mathbf{T})(\mathbf{G}\tilde{\mathbf{A}}_0\mathbf{T})^{-1} \\ &= \mathbf{G} \left(\mathbf{G}(\tilde{\mathbf{A}}_0 - \tilde{\mathbf{A}})\mathbf{T} \right) (\mathbf{G}\tilde{\mathbf{A}}_0\mathbf{T})^{-1} \\ &= \mathbf{G}(\mathbf{G}\Delta\tilde{\mathbf{A}}\mathbf{T})(\mathbf{G}\tilde{\mathbf{A}}_0\mathbf{T})^{-1}. \end{aligned} \quad (25)$$

It can be found from (14) that only the third row of $\tilde{\mathbf{A}}$ depends on \tilde{c} and \tilde{d} while the other two rows are constants. This specific structure can be reduced to simplify $\Delta\tilde{\mathbf{A}}$ as

$$\Delta\tilde{\mathbf{A}} = \begin{bmatrix} \mathbf{0}_{1 \times 3n} & \mathbf{0}_{1 \times 3n} & 0 \\ \mathbf{0}_{1 \times 3n} & \mathbf{0}_{1 \times 3n} & 0 \\ \mathbf{0}_{1 \times 3n} & -\Delta\tilde{c}\mathbf{C}_3\mathbf{M}^{-1}\mathbf{C} & \Delta\tilde{d}\mathbf{C}_3\mathbf{M}^{-1}\mathbf{F} \end{bmatrix}. \quad (26)$$

It is seen in (26) that the parameter deviations are located in the last row and input matrix \mathbf{T} has exactly the same structure as $\Delta\tilde{\mathbf{A}}$. Thus, \mathbf{G}^* can be further simplified as

$$\begin{aligned} \mathbf{G}^* &= \mathbf{G}(\mathbf{G}\Delta\tilde{\mathbf{A}}\mathbf{T})(\mathbf{G}\tilde{\mathbf{A}}_0\mathbf{T})^{-1} \\ &= \mathbf{G}\mathbf{G} \begin{bmatrix} 0 \\ 0 \\ \frac{\Delta\tilde{d}k_{\text{amp}}\mathbf{C}_3\mathbf{M}^{-1}\mathbf{F}}{\tau} \end{bmatrix} (\mathbf{G}\tilde{\mathbf{A}}_0\mathbf{T})^{-1} \\ &= g_3\Delta\tilde{d} \left(\frac{k_{\text{amp}}}{\tau} \right) \mathbf{G}\mathbf{C}_3\mathbf{M}^{-1}\mathbf{F} (\mathbf{G}\tilde{\mathbf{A}}_0\mathbf{T})^{-1} \end{aligned} \quad (27)$$

in which \mathbf{G}^* only depends on the deviation of the piezo-coefficient $\Delta\tilde{d}$. Since $\Delta\tilde{d} = \tilde{d}_0 - \tilde{d}$ and \tilde{d} is unknown, $\Delta\tilde{d}$ in (27) can be determined as $\Delta\tilde{d} = \tilde{d}_0 - \tilde{d}_l$. In order to express Ψ in terms of the parameter deviations, the same notations in (24) are employed (see Appendix B for further details)

$$\begin{aligned} \Psi &= \mathbf{G}\tilde{\mathbf{A}}\mathbf{T}(\mathbf{G}\tilde{\mathbf{A}}_0\mathbf{T})^{-1}\mathbf{G}\tilde{\mathbf{A}}_0\mathbf{H}_0\mathbf{Z}_0(t) - \mathbf{G}\tilde{\mathbf{A}}\mathbf{H}\mathbf{Z}(t) \\ &= \mathbf{G}\Delta\tilde{\mathbf{A}}\mathbf{H}_0\mathbf{Z}_0(t) + \mathbf{G}\tilde{\mathbf{A}}_0\Delta\mathbf{H}\mathbf{Z}_0(t) - \mathbf{G}\Delta\tilde{\mathbf{A}}\Delta\mathbf{H}\mathbf{Z}_0(t) \end{aligned}$$

$$\begin{aligned} &+ \mathbf{G}\tilde{\mathbf{A}}_0\mathbf{H}_0\Delta\mathbf{Z}(t) - \mathbf{G}\tilde{\mathbf{A}}_0\Delta\mathbf{H}\Delta\mathbf{Z}(t) - \mathbf{G}\Delta\tilde{\mathbf{A}}\mathbf{H}_0\Delta\mathbf{Z}(t) \\ &+ \mathbf{G}\Delta\tilde{\mathbf{A}}\Delta\mathbf{H}\Delta\mathbf{Z}(t) - (\mathbf{G}\tilde{\mathbf{A}}_0\mathbf{T})^{-1}\mathbf{G}\Delta\tilde{\mathbf{A}}\mathbf{T}\mathbf{G}\tilde{\mathbf{A}}_0\mathbf{H}_0\mathbf{Z}_0(t). \end{aligned} \quad (28)$$

It can be seen from (28) that Ψ depends on $\Delta\tilde{d}$, $\Delta\tilde{c}$ and $\Delta\mathbf{Z}$, which makes the switch term ϵ a function of parameter deviations and the modeling error. Furthermore, (23), (27) and (28) indicate that the proposed ϵ is state dependent rather than constant, which means that chatter can be reduced and the tracking performance can consequently be improved. If the bounds of $\Delta\tilde{d}$, $\Delta\tilde{c}$ and $\Delta\mathbf{Z}$ are known, \mathbf{G}^* and Ψ can be determined by (27) and (28). Therefore, the nonlinear control signal $u_f(t)$ can be obtained such that the proposed control can be applied to the plant at different frequencies without changing the initial parameters.

IV. NONLINEAR ESTIMATION BASED ON GENETIC ALGORITHMS

As discussed in the last section, the bounds of the parameter deviations are needed to determine $u_f(t)$. For a 1 DOF system, normal gradient methods can be used to estimate the parameters since the system governing equation can be represented as a linear parametric model. For a finite-element model with n DOFs, however, parameter vectors are nonlinearly coupled with \tilde{d} and \tilde{c} , which means the general gradient method cannot be used. For zero initial conditions, the transfer function representation of (7) is given by

$$\begin{aligned} H(s) &= \mathbf{\Gamma}(s\mathbf{I} - \mathbf{A})^{-1}\mathbf{B} \\ &= \frac{b_m s^m + b_{m-1} s^{m-1} + \dots + b_1 s + b_0}{s^n + a_{n-1} s^{n-1} + \dots + a_1 s + a_0} \end{aligned} \quad (29)$$

where $n - m = 2$. Here, we define $\theta_1 = \tilde{d}$, $\theta_2 = \tilde{c}$. The parametric model (29) can be written as

$$z = \varphi\phi = [\varphi_1 \ \varphi_2][\phi_1 \ \phi_2] \quad (30)$$

where φ is the coefficient vector and ϕ is the regressor

$$\begin{aligned} \varphi &= [b_m, \dots, b_0, a_{n-1}, \dots, a_0] \\ &= [f_m(\theta_1, \theta_2), \dots, f_0(\theta_1, \theta_2), g_{n-1}(\theta_1, \theta_2), \dots, g_0(\theta_1, \theta_2)]. \end{aligned}$$

Parameters θ_1 and θ_2 are coupled in φ via nonlinear equations f and g , which leaves the persistency excitation condition unsatisfied. In this case, Genetic Algorithms can be employed to solve nonlinear estimation problems. A Genetic Algorithm is a nonlinear estimation method that generates solutions to optimization problems using techniques inspired by natural evolution. It no longer requires the persistency excitation condition. Consider the canonical state-space representation of (29)

$$\begin{aligned} \dot{\mathbf{X}}_f &= \mathbf{A}_f(\boldsymbol{\theta})\mathbf{X}_f + \mathbf{B}_f I_c(t) \\ y_f &= \mathbf{C}_f(\boldsymbol{\theta})\mathbf{X}_f \end{aligned} \quad (31)$$

where $\boldsymbol{\theta} = [\theta_1, \theta_2]$ is the parameter vector; y_f is the output; \mathbf{A}_f and \mathbf{C}_f are nonlinear functions dependent on $\boldsymbol{\theta}$. The

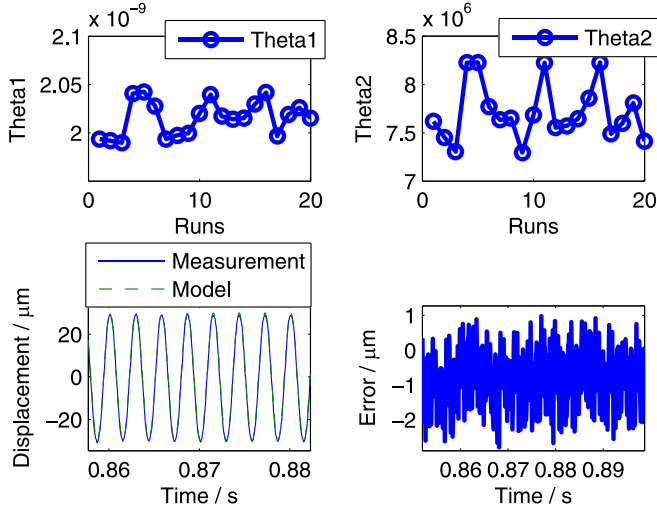


Fig. 3. Parameter estimation using a genetic algorithm at 350 Hz (20 runs).

estimation of (31) can be written as

$$\begin{aligned} \dot{\hat{\mathbf{X}}}_f &= \hat{\mathbf{A}}_f(\hat{\boldsymbol{\theta}})\hat{\mathbf{X}}_f + \mathbf{B}_f I_c(t) \\ \hat{y}_f &= \hat{\mathbf{C}}_f(\hat{\boldsymbol{\theta}})\hat{\mathbf{X}}_f. \end{aligned} \quad (32)$$

To apply the GA, each estimated parameter $\hat{\theta}_i$ is encoded as a string of binary numbers called a gene. Genes are cascaded to form a longer string $\hat{\mathbf{W}}$ called a chromosome. The estimation process applies the GA to search for the best chromosome $\hat{\mathbf{W}}$ so that $\hat{y}_f(k) \rightarrow y_f(k)$. This can be implemented by minimizing the cost function defined between experimental data and model calculations. Let

$$J(\boldsymbol{\theta}) = \sum_{i=1}^{N_l} \sum_{k=1}^{N_g} (y_i(k) - \hat{y}_i(k))^2 \quad (33)$$

where N_l is the number of chromosomes and N_g is the window size over which the errors will be accumulated. The parameters are assumed to be bounded in the following region:

$$\theta_{\min}^i \leq \theta_i \leq \theta_{\max}^i$$

where θ_{\min}^i and θ_{\max}^i are the limits of the i th element of the parameter vector. The selection of parent chromosomes is based on the fitness function, which can be expressed as

$$f_t(\boldsymbol{\theta}, t) = \frac{K}{\sum_{i=1}^{N_l} \sum_{k=1}^{N_g} (y_i(k) - \hat{y}_i(k))^2} \quad (34)$$

where K is defined as the gain value. The best parameter vector is chosen until the cost function satisfies the inequality $J(\boldsymbol{\theta}) < \delta$, in which δ is a small constant that defines the accuracy of the estimation. The population size is taken as $N_p = 120$ in this work, the crossover rate as $P_c = 0.7$, the mutation rate as $P_m = 0.002$, and the resolution of the parameter $p_i = 0.0001$. Estimation results at 350 Hz are illustrated in Fig. 3, in which the model prediction is compared with experimental measurement.

There are 20 total runs in the estimation process, and the mean values are taken as the parameters. It can be seen that θ_1 is

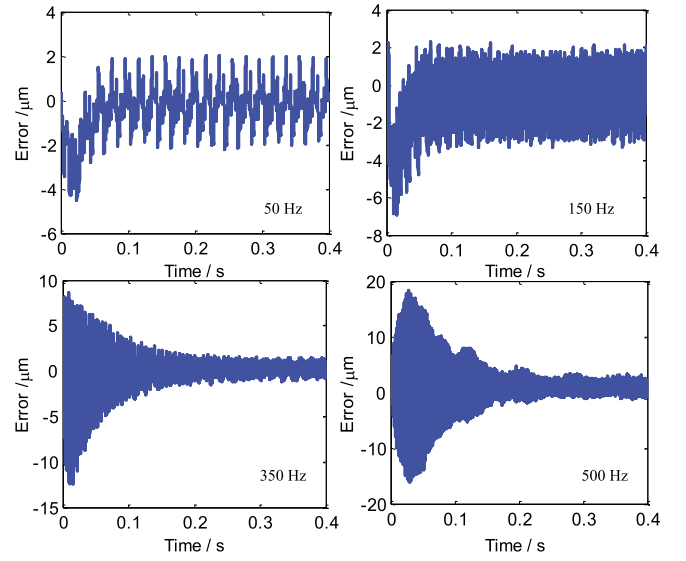


Fig. 4. Estimation errors at different frequencies.

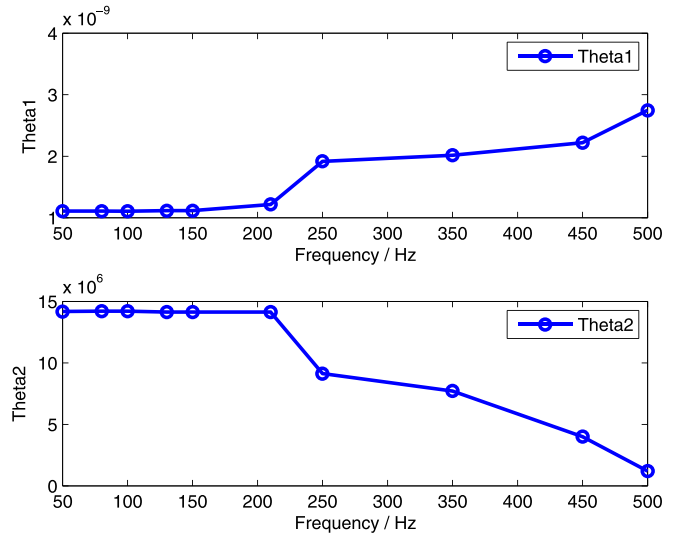


Fig. 5. Estimation of parameters at different frequencies.

around 2.02×10^{-9} and θ_2 is around 7.7×10^6 . The estimation error is bounded in a very small region. The estimation errors at different frequencies are illustrated in Fig. 4.

Here, we have selected four frequencies (50 Hz, 150 Hz, 350 Hz, and 500 Hz) in the range of 50 Hz to 500 Hz to demonstrate the actual value and the estimated value of displacement. It can be seen that the errors converge to a small region in finite time. Estimation results of parameters at different frequencies are illustrated in Fig. 5.

It is found in Fig. 5 that when the exciting frequency is relatively low (< 220 Hz), the parameters are almost constants. This explains why the linear constitutive model can be employed for control when the excitation frequency is low. When higher frequencies are involved, the parameters deviations increase with frequency. If the same controller based on initial parameters needs to be applied to the whole frequency range, the bounds of the variance illustrated in Fig. 5 need to be considered in (23) to make the controller robust enough for the parameter variances.

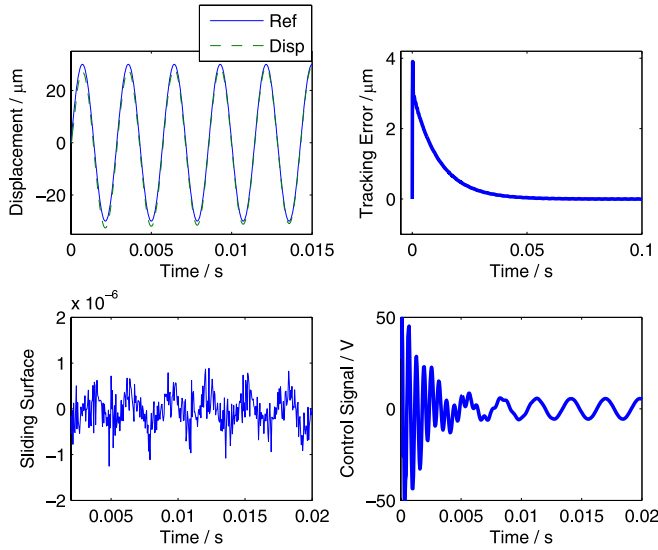


Fig. 6. Ideal case of the tracking (350 Hz, linear control only).

V. SIMULATIONS

It is assumed that there are no parameter deviations and the modeling error is zero. The nonlinear component $u_f(t)$ can be taken as 0. Simulation parameters of the sliding-mode controller are: $g_1 = 1.38 \times 10^6$, $g_2 = 15\,639$ and $g_3 = 0.05$. The sampling frequency is 20 kHz. Simulation results are shown in Fig. 6 for tracking a 350 Hz sinusoid signal. It can be seen from Fig. 6 that the tracking error goes to zero exponentially and the dynamics of the convergence are governed by the design vector \mathbf{G} . Also, the steady state value of the sliding surface is very close to zero but not exactly equal to zero. This error comes from the numerical calculation of state space (7). However, since the physical parameters of the beam are non-constants at different frequencies, the nonlinear component $u_f(t)$ should be employed to suppress the perturbation caused by the deviation.

It is now assumed that $\tilde{c} = 9 \times 10^6$, $\tilde{d} = 2.406 \times 10^{-9}$, $\tilde{c}_0 = 7.57 \times 10^6$ and $\tilde{d}_0 = 1.916 \times 10^{-9}$. Simulation results are shown in Fig. 7 when the linear control in (17) is used. It can be seen that the sliding surface is much greater than zero. Consequently, the absolute value of the system output becomes much greater than the reference signal. The control input plotted in Fig. 7 is saturated and the state variables can no longer reach the sliding surface. Actually, the output would go to infinity if there was no saturation voltage limit in the simulation. In order to suppress the perturbations caused by parameter deviations, the proposed nonlinear control in (18) is employed. The bounds of the parameters are $\tilde{c}_l = 1.0 \times 10^6$, $\tilde{d}_l \times 1.0 \times 10^{-9}$, $\tilde{c}_u = 16 \times 10^6$, $\tilde{d}_u = 3.0 \times 10^{-9}$. The bounds of $\Delta \mathbf{Z}$ can be determined via physical measurement. We define the modeling error of the deflection as

$$\Delta r = \frac{\|z_m - z_p\|}{\|z_m\|}$$

where z_m and z_p are the modeling state and physical measurement. The bounds of $\Delta \mathbf{Z}$ can be calculated as $\Delta \mathbf{Z}_b = \Delta r \mathbf{Z}_{0b}$, where \mathbf{Z}_{0b} is the state bound of the model.

From (23) the proposed switching gain is state dependent rather than constant, which means ϵ will not be over magnified

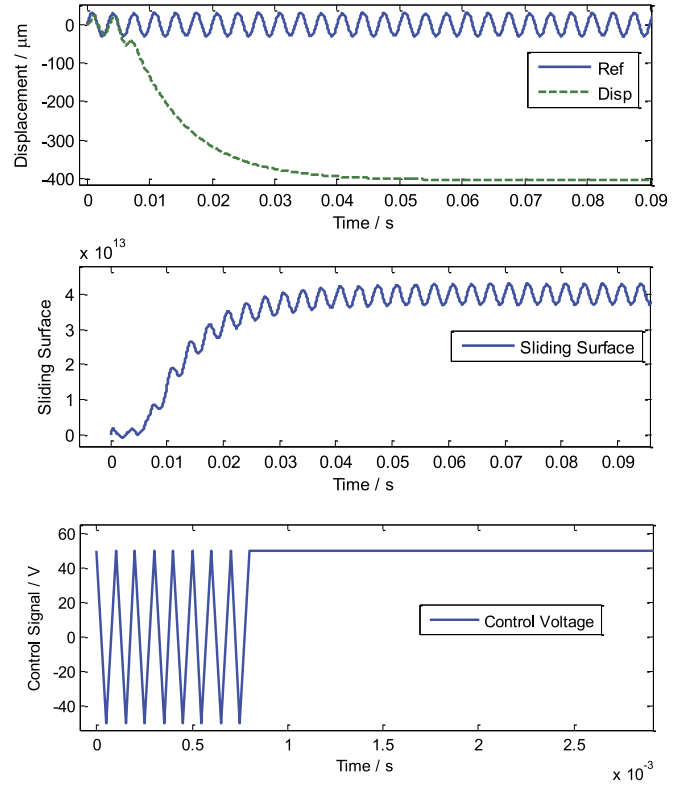


Fig. 7. Tracking result when $\tilde{c} \neq \tilde{c}_0$, $\tilde{d} \neq \tilde{d}_0$ (linear control only, 350 Hz).

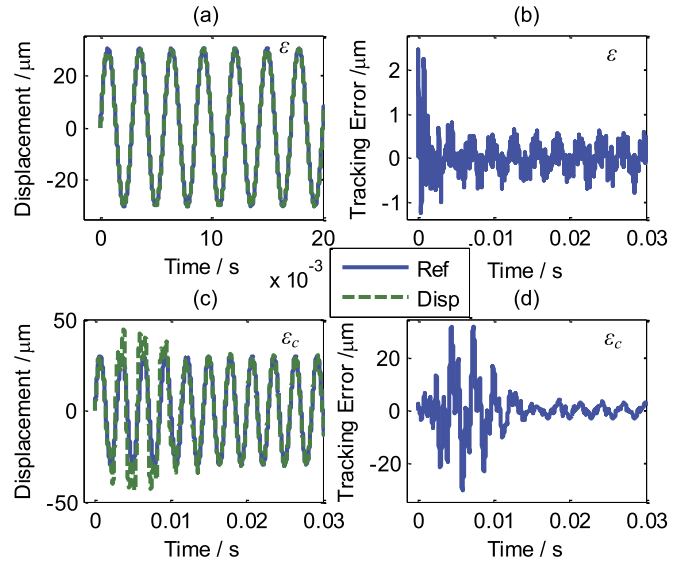


Fig. 8. Comparative results when ϵ and ϵ_c are used (350 Hz).

when the deviation is relatively small. The constant ϵ_c is used here as a comparison with the proposed nonlinear control $u_f(t)$. According to (23), the value of ϵ_c should be at least the maximum of ϵ . Simulation results are shown in Fig. 8. In Fig. 8, the first two subplots [(a), (b)] are based on ϵ and [(c), (d)] are based on ϵ_c . The control voltage and current are plotted in Fig. 9. The first two subplots [(a), (b)] are the control voltage and the last two subplots [(c), (d)] are the excitation current applied to the coil. It can be seen from Fig. 8 that the system can be stabilized when nonlinear control is applied to the system.

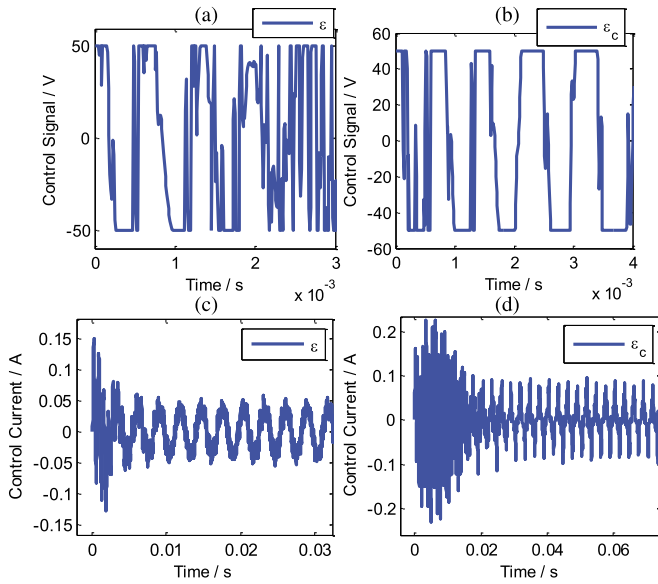


Fig. 9. Control voltage and current when ϵ and ϵ_c are used (350 Hz).

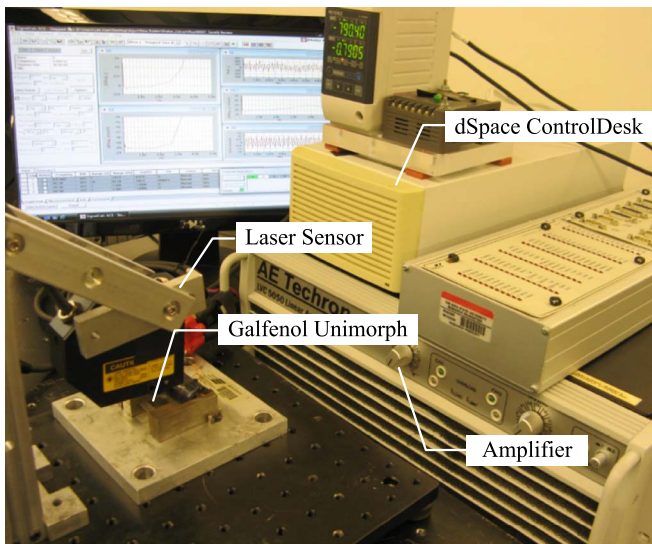


Fig. 10. Experimental setup used to implement the controller.

Also, from the voltage plots in Fig. 9 it is observed that the switching frequency based on ϵ is faster than ϵ_c . This enables the system to track the external signal with high speed and high accuracy. Fig. 8(b)–(d) show that the tracking error is small. Since the magnitude of ϵ changes according to the system states, both transient error and steady state error in subplot (b) are much smaller than the error in (d). Also, the system can be stabilized much faster when ϵ is used than ϵ_c since the transient response takes less time in subplot Fig. 8(b).

VI. EXPERIMENTAL RESULTS

A linear PI controller is chosen to compare the performance with the proposed nonlinear sliding-mode control. The controller is implemented with dSpace ControlDesk, as illustrated in Fig. 10. The geometric parameters for the unimorph can be found in [20]. The control parameters for the sliding-mode controller are: $g_1 = 12000$, $g_2 = 139$ and $g_3 = 0.01$. For the PI

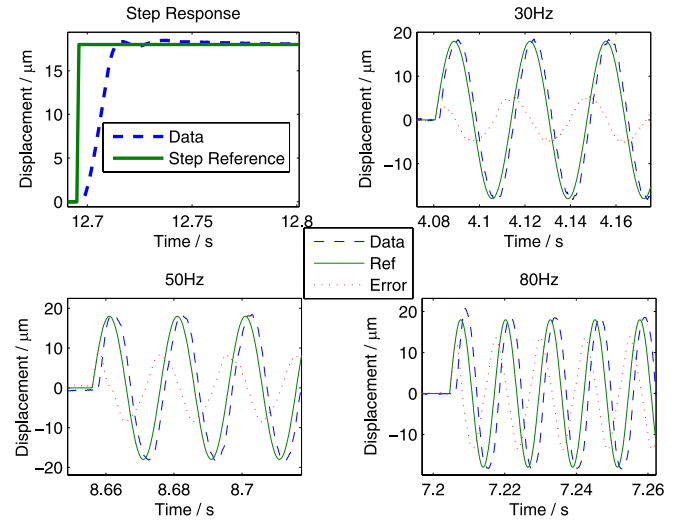


Fig. 11. Tracking results of linear PI control.

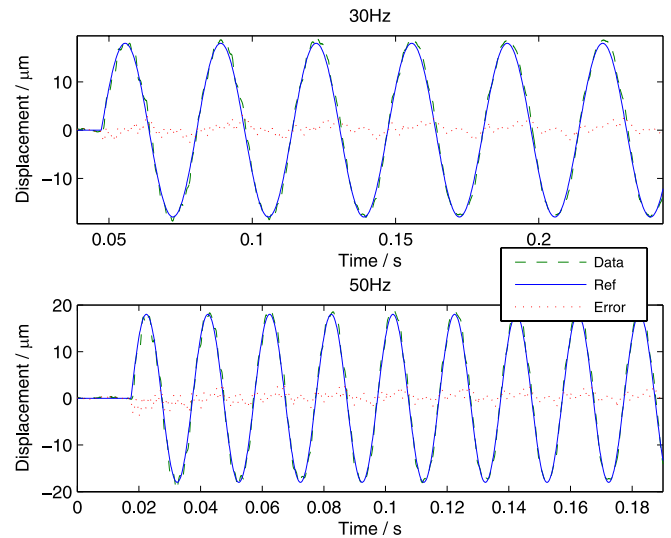


Fig. 12. Tracking results of sliding-mode control (30 Hz, 50 Hz).

controller, $K_p = 0.008$ and $K_i = 0.46$. Sampling frequencies for both controllers are 20 kHz. The tracking results based on PI control are illustrated in Fig. 11. Parameters of the controller are obtained from the step response. It can be seen from the step response in Fig. 11 that the steady state error is almost zero and there is no obvious overshoot. However, the dynamic response of the system is limited due to the nonlinearity of the Galfenol alloy. The settling time is more than 0.05 s, which makes the controller too slow to track high frequency signals.

Tracking results of the nonlinear sliding-mode control are illustrated in Figs. 12–16, in which dynamic frequencies range from 30 Hz–400 Hz. Initial parameters are estimated from a quasi static test. Since the parameters change frequency dependently, the nonlinear term in (18) is employed to guarantee system stability without changing the initial parameters. Parameter bounds estimated in Section III are considered by using (23). In Figs. 12 and 13, the reference frequencies chosen are the same as in the PI control. It can be seen that unlike linear control, the proposed controller can track both the magnitude and phase of the reference.

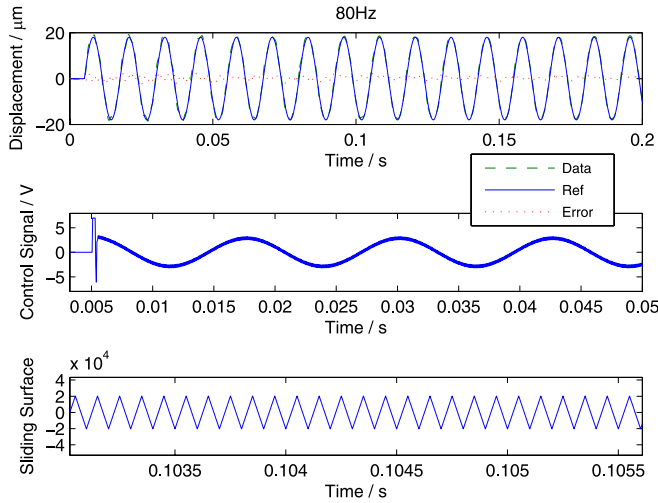


Fig. 13. Tracking results of sliding-mode control (80 Hz).

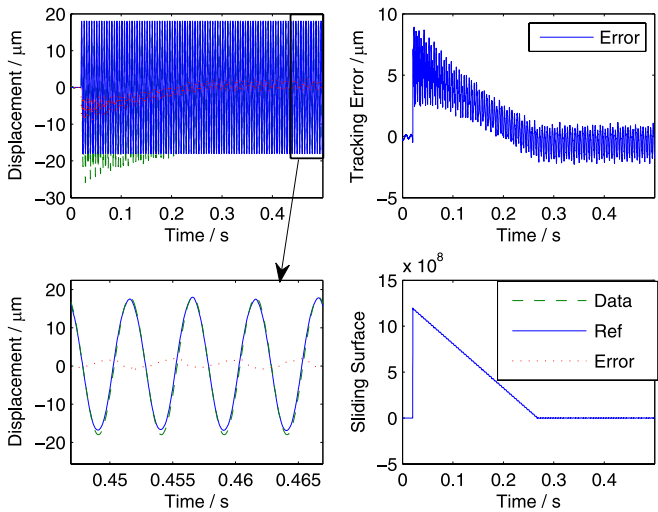


Fig. 14. Tracking results of sliding-mode control (200 Hz).

From Fig. 13 it is observed that the sliding surface $s(t)$ is nonzero, but a periodic wave with zero expected value. This is because of the limit of sampling frequency. Ideally, if the sampling frequency goes to infinity, the sliding surface is absolutely zero and the reference signal can be tracked completely. Experimental results at higher frequencies are illustrated in Figs. 14–16. It is found that tracking errors in transient response are relatively larger than the errors at steady state. It is also observed that the tracking errors of the sliding-mode controller hardly change when the frequencies are relatively low. For higher frequencies, both the steady state errors and the transient errors increase as frequency increases. Since the transient responses take longer at high frequencies, it is observed from Figs. 15 and 16 that transient responses still remain even when the system reaches the sliding surface. This explains the drifts and decays in these tracking errors.

The convergence of error from initial value to steady state value is consistent with the convergence of the sliding surface. Initially, the cantilever system runs in the state far away from the sliding surface. Consequently, large errors are observed. The control signal starts to work due to the existence of tracking

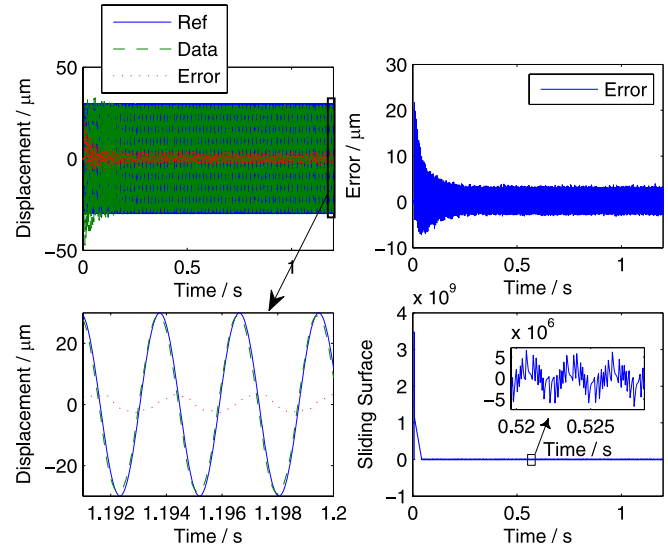


Fig. 15. Tracking results of sliding-mode control (350 Hz).

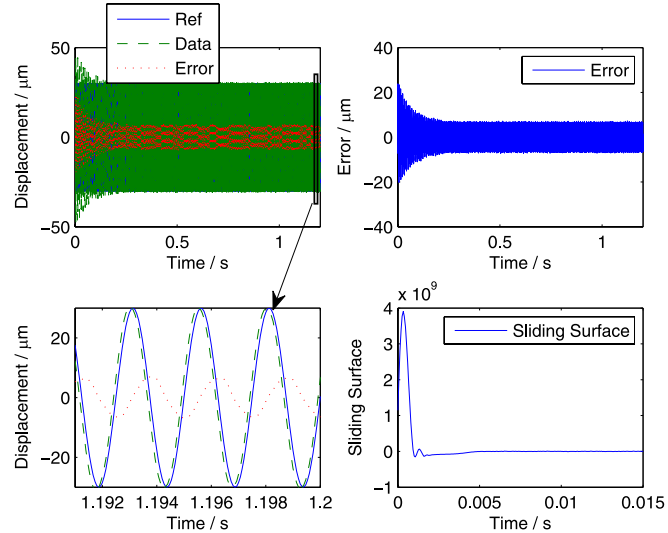


Fig. 16. Tracking results of sliding-mode control (400 Hz).

errors, forcing the system to move toward the surface. Once it reaches the surface, the system maintains there under the control of the sliding mode, meaning the reference signal has been tracked in a steady state. This moving process can be observed from the trajectories of both the tracking errors and the sliding surfaces.

In low frequency applications, we notice that tracking errors in transient responses are almost equal to the errors in steady state. No moving trajectories can be observed. This is because the system reaches the sliding surface very quickly, so the whole moving process happens in a very short period. It is also observed from Figs. 14–16 that the tracking error amplitude increases as frequency increases. This is because the accuracy of the control mostly depends on the equivalent control signal $V_{eq}(t)$, which is a function of initial parameters $\tilde{\mathbf{A}}_0$ and \mathbf{H}_0 . Since $\tilde{\mathbf{A}}_0$ and \mathbf{H}_0 are approximated from a quasi static test, the tracking is more accurate when the physical parameters are close to the initial approximation. The switch control $u_f(t)$ is employed in (18) to guarantee system stability when the

physical parameters $\tilde{\mathbf{A}}$ and \mathbf{H} are far away from the initial values. It can be seen from Fig. 16 that although the tracking error increases, the system still remains in stability even the real parameters go beyond the initial values (see Fig. 5).

VII. CONCLUSION

A model based sliding-mode control is developed for a Galfenol cantilever beam. The dynamic model is developed by coupling the structural dynamics of the composite beam with the magnetostriction generated by the Galfenol layer. It is found that structural damping and the piezo-coefficient vary at different frequencies. In order to apply the controller to the system without changing the initial parameters, a nonlinear component is developed in the sliding-mode control to guarantee system stability, even if the physical parameters vary frequency dependently. A linear PI control is chosen as a comparative experiment. It is shown that that significant performance enhancements are achieved by the proposed control. Moreover, it is found that system instability is induced if only an equivalent control is used. The proposed nonlinear control works at frequencies up to 400 Hz.

APPENDIX A SYSTEM MATRICES

System matrices can be calculated as

$$\begin{aligned} \mathbf{m}_e^u &= \frac{l_e \rho A}{2} \int_{-1}^1 \mathbf{N}^T \cdot \mathbf{N} d\xi, & \mathbf{m}_e^v &= \frac{l_e \rho A}{2} \int_{-1}^1 \mathbf{H}^T \cdot \mathbf{H} d\xi \\ \mathbf{c}_e^u &= \frac{l_e c A}{2} \int_{-1}^1 \mathbf{N}^T \cdot \mathbf{N} d\xi, & \mathbf{c}_e^v &= \frac{l_e c A}{2} \int_{-1}^1 \mathbf{H}^T \cdot \mathbf{H} d\xi \\ \mathbf{k}_e^v &= \frac{8EI}{l_e^3} \int_{-1}^1 \left(\frac{d^2 \mathbf{H}}{d\xi^2} \right)^T \frac{d^2 \mathbf{H}}{d\xi^2} d\xi, & \mathbf{k}_e^u &= EA l_e \mathbf{B}^T \cdot \mathbf{B} \end{aligned}$$

$$\begin{aligned} \mathbf{k}_e^{uv} &= \frac{2EQ}{l_e} \int_{-1}^1 \left(\frac{d^2 \mathbf{H}}{d\xi^2} \right)^T \mathbf{B} d\xi, & \mathbf{f}^u &= \frac{E_g b l_e \tilde{N} I_c}{2} \int_{-1}^1 \int_{t_g}^1 \mathbf{B} dz d\xi \\ \mathbf{f}^v &= \frac{2E_g b \tilde{N} I_c}{l_e} \int_{-1}^1 \int_{t_g}^1 z \frac{d^2 \mathbf{H}}{d\xi^2} dz d\xi. \end{aligned} \quad (35)$$

The definitions of the shape functions and the geometries in the matrices can be found in [20]. Equations (4), (5), and (8) are connected from the calculations of the load matrices in (35).

APPENDIX B DERIVATION OF Ψ

Notations in (24) can be employed to express Ψ in terms of parameter deviations

$$\begin{aligned} \Psi &= \mathbf{G} \tilde{\mathbf{A}} \mathbf{T} \left(\mathbf{G} \tilde{\mathbf{A}}_0 \mathbf{T} \right)^{-1} \mathbf{G} \tilde{\mathbf{A}}_0 \mathbf{H}_0 \mathbf{Z}_0(t) - \mathbf{G} \tilde{\mathbf{A}} \mathbf{H} \mathbf{Z}(t) \\ &= \left(\mathbf{G} \tilde{\mathbf{A}}_0 \mathbf{T} \right)^{-1} \mathbf{G} \left(\tilde{\mathbf{A}}_0 - \Delta \tilde{\mathbf{A}} \right) \mathbf{T} \mathbf{G} \tilde{\mathbf{A}}_0 \mathbf{H}_0 \mathbf{Z}_0(t) \\ &\quad - \left(\mathbf{G} \tilde{\mathbf{A}}_0 \mathbf{T} \right)^{-1} \mathbf{G} \tilde{\mathbf{A}}_0 \mathbf{T} \mathbf{G} \left(\tilde{\mathbf{A}}_0 - \Delta \tilde{\mathbf{A}} \right) \left(\mathbf{H}_0 - \Delta \mathbf{H} \right) \\ &\quad \times \left(\mathbf{Z}_0(t) - \Delta \mathbf{Z}(t) \right) \\ &= \mathbf{G} \Delta \tilde{\mathbf{A}} \mathbf{H}_0 \mathbf{Z}_0(t) + \mathbf{G} \tilde{\mathbf{A}}_0 \Delta \mathbf{H} \mathbf{Z}_0(t) - \left(\mathbf{G} \tilde{\mathbf{A}}_0 \mathbf{T} \right)^{-1} \\ &\quad \times \mathbf{G} \Delta \tilde{\mathbf{A}} \mathbf{T} \mathbf{G} \tilde{\mathbf{A}}_0 \mathbf{H}_0 \mathbf{Z}_0(t) \\ &\quad - \mathbf{G} \Delta \tilde{\mathbf{A}} \Delta \mathbf{H} \mathbf{Z}_0(t) + \mathbf{G} \left(\tilde{\mathbf{A}}_0 - \Delta \tilde{\mathbf{A}} \right) \left(\mathbf{H}_0 - \Delta \mathbf{H} \right) \Delta \mathbf{Z}(t) \\ &= \mathbf{G} \Delta \tilde{\mathbf{A}} \mathbf{H}_0 \mathbf{Z}_0(t) + \mathbf{G} \tilde{\mathbf{A}}_0 \Delta \mathbf{H} \mathbf{Z}_0(t) - \left(\mathbf{G} \tilde{\mathbf{A}}_0 \mathbf{T} \right)^{-1} \\ &\quad \times \mathbf{G} \Delta \tilde{\mathbf{A}} \mathbf{T} \mathbf{G} \tilde{\mathbf{A}}_0 \mathbf{H}_0 \mathbf{Z}_0(t) \\ &\quad - \mathbf{G} \Delta \tilde{\mathbf{A}} \Delta \mathbf{H} \mathbf{Z}_0(t) + \mathbf{G} \tilde{\mathbf{A}}_0 \mathbf{H}_0 \Delta \mathbf{Z}(t) - \mathbf{G} \tilde{\mathbf{A}}_0 \Delta \mathbf{H} \Delta \mathbf{Z}(t) \\ &\quad - \mathbf{G} \Delta \tilde{\mathbf{A}} \mathbf{H}_0 \Delta \mathbf{Z}(t) + \mathbf{G} \Delta \tilde{\mathbf{A}} \Delta \mathbf{H} \Delta \mathbf{Z}(t) \end{aligned}$$

where $\Delta \tilde{\mathbf{A}} \mathbf{H}_0$ shown at the bottom of the page.

$$\begin{aligned} \Delta \tilde{\mathbf{A}} \mathbf{H}_0 &= \begin{bmatrix} \underbrace{1 \times 3n}_{\mathbf{0}} & \underbrace{1 \times 3n}_{\mathbf{0}} & 0 \\ \underbrace{1 \times 3n}_{\mathbf{0}} & \underbrace{1 \times 3n}_{\mathbf{0}} & 0 \\ \Delta \tilde{c} \mathbf{C}_3 \mathbf{M}^{-1} \mathbf{C} \mathbf{M}^{-1} \mathbf{K} & \Delta \tilde{c} \tilde{c}_0 \mathbf{C}_3 \mathbf{M}^{-1} \mathbf{C} \mathbf{M}^{-1} \mathbf{C} & -\mathbf{C}_3 \mathbf{M}^{-1} \left(\Delta \tilde{c} \tilde{d}_0 \mathbf{C} \mathbf{M}^{-1} \mathbf{F} + \frac{\Delta \tilde{d}}{\tau} \mathbf{F} \right) \end{bmatrix} \\ \Delta \tilde{\mathbf{A}} \Delta \mathbf{H} &= \begin{bmatrix} \underbrace{1 \times 3n}_{\mathbf{0}} & \underbrace{1 \times 3n}_{\mathbf{0}} & 0 \\ \underbrace{1 \times 3n}_{\mathbf{0}} & \underbrace{1 \times 3n}_{\mathbf{0}} & 0 \\ \mathbf{0} & \Delta \tilde{c}^2 \mathbf{C}_3 \mathbf{M}^{-1} \mathbf{C} \mathbf{M}^{-1} \mathbf{C} & -\Delta \tilde{c} \Delta \tilde{d} \mathbf{C}_3 \mathbf{M}^{-1} \mathbf{C} \mathbf{M}^{-1} \mathbf{F} \end{bmatrix} \\ \tilde{\mathbf{A}}_0 \Delta \mathbf{H} &= \begin{bmatrix} \underbrace{1 \times 3n}_{\mathbf{0}} & \underbrace{1 \times 3n}_{\mathbf{0}} & 0 \\ \mathbf{0} & -\Delta \tilde{c} \mathbf{C}_3 \mathbf{M}^{-1} \mathbf{C} & \Delta \tilde{d} \mathbf{C}_3 \mathbf{M}^{-1} \mathbf{F} \\ \mathbf{0} & \Delta \tilde{c} \tilde{c}_0 \mathbf{C}_3 \mathbf{M}^{-1} \mathbf{C} \mathbf{M}^{-1} \mathbf{C} & -\Delta \tilde{d} \tilde{c}_0 \mathbf{C}_3 \mathbf{M}^{-1} \mathbf{C} \mathbf{M}^{-1} \mathbf{F} \end{bmatrix} \\ \mathbf{G} \Delta \tilde{\mathbf{A}} \mathbf{T} &= g_3 \Delta \tilde{d} \left(\frac{k_{\text{amp}}}{\tau} \right) \mathbf{C}_3 \mathbf{M}^{-1} \mathbf{F} \end{aligned}$$

REFERENCES

- [1] A. Sadighi and W. J. Kim, "Sensorless control of a novel linear magnetostrictive motor," *IEEE Trans. Ind. Appl.*, vol. 47, no. 2, pp. 736–743, Mar./Apr. 2011.
- [2] J. Atulasimha and A. B. Flatau, "A review of magnetostrictive iron-gallium alloys," *Smart Mater. Struct.*, vol. 20, no. 4, Mar. 2011, Art. ID. 043001.
- [3] H. Aschemann and D. Schindele, "Comparison of model-based approaches to the compensation of hysteresis in the force characteristic of pneumatic muscles," *IEEE Trans. Ind. Electron.*, vol. 61, no. 7, pp. 3620–3629, Jul. 2014.
- [4] S. Chakrabarti and M. Dapino, "A dynamic model for a displacement amplified magnetostrictive driver for active mounts," *Smart Mater. Struct.*, vol. 19, no. 5, Mar. 2010, Art. ID. 055099.
- [5] X. Chen, C. Y. Su, and T. Fukuda, "Adaptive control for the systems preceded by hysteresis," *IEEE Trans. Autom. Control*, vol. 53, no. 4, pp. 1019–1025, May 2008.
- [6] X. Chen and T. Hisayama, "Adaptive sliding-mode position control for piezo-actuated stage," *IEEE Trans. Ind. Electron.*, vol. 55, no. 11, pp. 3927–3934, Nov. 2008.
- [7] P. G. Evans and M. Dapino, "Dynamic model for 3-D magnetostrictive transducers," *IEEE Trans. Magn.*, vol. 47, no. 1, pp. 221–230, Jan. 2011.
- [8] M. Grossard, M. Boukallel, N. Chaillet, and C. Rotinat-Libersa, "Modeling and robust control strategy for a control-optimized piezoelectric microgripper," *IEEE/ASME Trans. Mechatronics*, vol. 16, no. 4, pp. 674–683, Aug. 2011.
- [9] G. Y. Gu, Z. Li, L. M. Zhu, and C. Y. Su, "A comprehensive dynamic modeling approach for giant magnetostrictive material actuators," *Smart Mater. Struct.*, vol. 22, no. 12, Nov. 2013, Art. ID. 125005.
- [10] G. Y. Gu, L. M. Zhu, and C. Y. Su, "Modeling and compensation of asymmetric hysteresis nonlinearity for piezoceramic actuators with a modified Prandtl-Ishlinskii model," *IEEE Trans. Ind. Electron.*, vol. 61, no. 3, pp. 1583–1595, Mar. 2014.
- [11] G. L. Hwang, Y. M. Chen, and C. Jan, "Trajectory tracking of large-displacement piezoelectric actuators using a nonlinear observer-based variable structure control," *IEEE Trans. Control Syst. Technol.*, vol. 13, no. 1, pp. 56–66, Jan. 2005.
- [12] J. H. Lee, P. E. Allaire, G. Tao, and X. R. Zhang, "Integral sliding-mode control of a magnetically suspended balance beam: Analysis, simulation, and experiment," *IEEE/ASME Trans. Mechatronics*, vol. 6, no. 3, pp. 338–346, Sep. 2001.
- [13] H. C. Liwa, B. Shirinzadeh, and J. Smith, "Enhanced sliding mode motion tracking control of piezoelectric actuators," *Sens. Actuators A, Phys.*, vol. 138, no. 1, pp. 194–202, Jul. 2007.
- [14] J. A. McMahan, Jr., J. H. Crews, and R. C. Smith, "Inversion algorithms for the homogenized energy model for hysteresis in ferroelectric and shape memory alloy compounds," *J. Intell. Mater. Syst. Struct.*, vol. 24, no. 15, pp. 1796–1821, Oct. 2013.
- [15] J. Nealis and R. C. Smith, "Model-Based robust control design for magnetostrictive transducers operating in hysteretic and nonlinear regimes," *IEEE Trans. Control Syst. Technol.*, vol. 15, no. 1, pp. 22–39, Jan. 2007.
- [16] W. S. Oates, P. G. Evans, R. C. Smith, and M. Dapino, "Experimental implementation of a hybrid nonlinear control design for magnetostrictive actuators," *Trans. ASME, J. Dyn. Syst., Meas. Control*, vol. 131, no. 4, Jul. 2009, Art. ID. 041004.
- [17] W. S. Oates and R. C. Smith, "Optimal tracking using magnetostrictive actuators operating in nonlinear and hysteretic regimes," *Trans. ASME, J. Dyn. Syst., Meas. Control*, vol. 131, no. 3, May 2009, Art. ID. 031001.
- [18] W. Panusittikorn and P. I. Ro, "Modeling and control of a magnetostrictive tool servo system," *Trans. ASME, J. Dyn. Syst., Meas. Control*, vol. 130, no. 3, May 2008, Art. ID. 031003.
- [19] M. J. Shirazi, H. Salarieh, A. Alasty, and R. Shabani, "Tip tracking control of a micro-cantilever Timoshenko beam via piezoelectric actuator," *J. Vib. Control*, vol. 19, no. 10, pp. 1561–1574, Jul. 2013.
- [20] L. Shu, L. Headings, M. Dapino, D. F. Chen, and Q. G. Lu, "Nonlinear model of Galfenol cantilevered unimorphs considering full magnetoelastic coupling," *J. Intell. Mater. Syst. Struct.*, vol. 25, no. 2, pp. 187–203, Jan. 2014.
- [21] X. B. Tan and J. S. Baras, "Modeling and control of hysteresis in magnetostrictive actuators," *Automatica*, vol. 40, no. 9, pp. 1469–1480, Sep. 2004.
- [22] B. Vaseghi, D. Matheka, S. Rahman, and A. Knight, "Parameter optimization and study of inverse J-A hysteresis model," *IEEE Trans. Magn.*, vol. 49, no. 5, pp. 1637–1640, May 2013.
- [23] W. Wang, K. Nonami, and Y. Ohira, "Model reference sliding mode control of small helicopter X.R.B based on vision," *Int. J. Adv. Rob. Syst.*, vol. 5, no. 3, pp. 235–242, Sep. 2008.
- [24] Z. H. Wang, Q. Z. Zou, L. Faidley, and G. Y. Kim, "Dynamics compensation and rapid resonance identification in ultrasonic-vibration-assisted microforming system using magnetostrictive actuator," *IEEE/ASME Trans. Mechatronics*, vol. 16, no. 3, pp. 489–497, Jun. 2011.
- [25] S. L. Xiao and Y. M. Li, "Modeling and high dynamic compensating the rate-dependent hysteresis of piezoelectric actuators via a novel modified inverse Preisach model," *IEEE Trans. Control Syst. Technol.*, vol. 21, no. 5, pp. 1549–1557, Sep. 2013.
- [26] S. L. Xiao and Y. M. Li, "Optimal design, fabrication, and control of an XY micropositioning stage driven by electromagnetic actuators," *IEEE Trans. Ind. Electron.*, vol. 60, no. 10, pp. 4613–4626, Oct. 2013.
- [27] J. X. Xu and K. Abidi, "Discrete-time output integral sliding-mode control for a piezomotor-driven linear motion stage," *IEEE Trans. Ind. Electron.*, vol. 55, no. 11, pp. 3917–3926, Nov. 2008.
- [28] J. X. Xu, D. Q. Huang, V. Venkataramanan, and T. C. T. Huynh, "Extreme precise motion tracking of piezoelectric positioning stage using sampled-data iterative learning control," *IEEE Trans. Control Syst. Technol.*, vol. 21, no. 4, pp. 1432–1439, Jul. 2013.
- [29] Q. S. Xu, "Digital sliding-mode control of piezoelectric micropositioning system based on input-output model," *IEEE Trans. Ind. Electron.*, vol. 61, no. 10, pp. 5517–5526, Oct. 2014.
- [30] Q. S. Xu and Y. M. Li, "Micro/nanopositioning using model predictive output integral discrete sliding mode control," *IEEE Trans. Ind. Electron.*, vol. 59, no. 2, pp. 1161–1170, Feb. 2012.
- [31] X. H. Yu and G. R. Chen, "Discretization behaviors of equivalent control based sliding-mode control systems," *IEEE Trans. Autom. Control*, vol. 48, no. 9, pp. 1641–1646, Sep. 2003.
- [32] J. Zhang, E. Merced, N. Sepulveda, and X. B. Tan, "Modeling and inverse compensation of nonmonotonic hysteresis in VO₂-coated microactuators," *IEEE/ASME Trans. Mechatronics*, vol. 19, no. 2, pp. 579–588, Apr. 2014.



Liang Shu received the B.S. degree in electrical engineering and automation from China Three Gorges University, Yichang, China, in 2005, and the M.S. and Ph.D. degrees in mechanical engineering from Wuhan University of Technology, Wuhan, China, in 2008 and 2011, respectively.

He was a Research Assistant in mechanical engineering at The Ohio State University, Columbus, OH, USA, from September 2008 to January 2011. He is currently an Associate Professor at Wenzhou University, Wenzhou, China.

His research interests include smart materials and structures, mechatronics and dynamic control.

Dr. Shu is a Senior Member of the Chinese Mechanical Engineering Society.



Marcelo Dapino received the Engineering Diploma from the University of Uruguay, Montevideo, Uruguay, in 1994 and the Ph.D. degree from Iowa State University, Ames, IA, USA, in 1999.

He is the Honda R&D Americas Designated Chair in Engineering at The Ohio State University, Columbus, OH, USA, where he is a Professor in the Department of Mechanical and Aerospace Engineering. He serves as Director of the Honda-OSU Mobility Innovation Exchange, as Associate Director for Research of the Smart Vehicle Concepts Center (a National Science Foundation Industry/University Cooperative Research Center), and is a Senior Fellow of The Ohio State University Center for Automotive Research. His research interests are design and manufacture of smart material systems.

Prof. Dapino is a member of the Executive Committee of the American Society of Mechanical Engineers (ASME) Aerospace Division and has led the organization of major ASME and Society for Optical Engineering (SPIE) conferences.



Guichu Wu was born in 1957 in Wenzhou, China. He received the B.S. degree in physics from Wenzhou University, Wenzhou, in 1980.

Since 1986, he has been with Wenzhou University, where he is currently a Professor of electrical engineering and the Director of the Key Laboratory of Low-Voltage Apparatus Intellectual Technology. His research interests include dynamic modeling and control and electromagnetic systems.

Prof. Wu is a Senior Member of the Chinese Society for Electrical Engineering.



Dingfang Chen received the B.S. degree in mechanical engineering from Huazhong University of Science and Technology, Wuhan, China in 1969.

Since 1979, he has been with Wuhan University of Technology, Wuhan, where he is currently a Professor of mechanical engineering. His research interests include intelligent manufacturing and control and finite-element method.